



Asteroid Diameters and Albedos from NEOWISE Reactivation Mission Years Six and Seven

Joseph R. Masiero¹ , A. K. Mainzer², J. M. Bauer³ , R. M. Cutri¹ , T. Grav², E. Kramer⁴ , J. Pittichová⁴, and E. L. Wright⁵

¹ Caltech/IPAC, 1200 E California Boulevard, MC 100-22, Pasadena, CA 91125, USA; jmasiero@ipac.caltech.edu

² Lunar and Planetary Laboratory, University of Arizona, Tucson, AZ, 85721, USA

³ University of Maryland, College Park, MD, 20742, USA

⁴ Jet Propulsion Laboratory/California Institute of Technology, Pasadena, CA 91109, USA

⁵ University of California, Los Angeles, CA 90095, USA

Received 2021 May 5; revised 2021 July 15; accepted 2021 July 15; published 2021 August 12

Abstract

We present diameters and albedos computed for the near-Earth and main belt asteroids (MBAs) observed by the Near-Earth Object Wide-field Infrared Survey Explorer (NEOWISE) spacecraft during the sixth and seventh years of its Reactivation mission. These diameters and albedos are calculated from fitting thermal models to NEOWISE observations of 199 near-Earth objects (NEOs) and 5851 MBAs detected during the sixth year of the survey and 175 NEOs and 5861 MBAs from the seventh year. Comparisons of the NEO diameters derived from Reactivation data with those derived from the WISE cryogenic mission data show a $\sim 30\%$ relative uncertainty. This larger uncertainty compared to data from the cryogenic mission is due to the need to assume a beaming parameter for the fits to the shorter-wavelength data that the Reactivation mission is limited to. We also present an analysis of the orbital parameters of the MBAs that have been discovered by NEOWISE during Reactivation, finding that these objects tend to be on orbits that result in their perihelia being far from the ecliptic, and thus missed by other surveys. To date, the NEOWISE Reactivation survey has provided thermal fits of 1415 unique NEOs. Including the mission phases before spacecraft hibernation increases the count of unique NEOs characterized to 1845 from WISE's launch to the present.

Unified Astronomy Thesaurus concepts: Asteroids (72); Near-Earth objects (1092); Infrared astronomy (786)

Supporting material: machine-readable tables

1. Introduction

Surveying in its Reactivated mission since 2013 December 13, the Near-Earth Object Wide-field Infrared Survey Explorer (NEOWISE) has obtained over 14 epochs of observations of the sky at thermal infrared wavelengths. Included in the archived, publicly accessible data from the survey are over one million photometric and astrometric measurements of asteroids and comets. These data provide a unique resource for studying the small bodies of our solar system, as well as the time-variable infrared sky.

The NEOWISE mission (Mainzer et al. 2014) makes use of the Wide-field Infrared Survey Explorer (WISE) spacecraft (Wright et al. 2010), which follows a Sun-synchronous polar orbit above Earth's terminator, scanning rings around the sky over the course of each orbit. As the survey progresses, the same area of sky is repeatedly imaged over the course of ~ 24 hr, allowing moving objects to be distinguished from background sources, and for the detection and discovery of new near-Earth objects (NEOs). Images and extracted source catalogs from these data are archived and accessible at the NASA/IPAC Infrared Science Archive (IRSA).⁶ The NEOWISE Explanatory Supplement (Cutri et al. 2015) provides a comprehensive overview of the mission and data products.

The NEOWISE infrared observations provide measurements of the thermal emission from a large number of small bodies in the inner solar system. The data, when analyzed by means of thermal modeling techniques, allow us to constrain the size of these bodies, as well as their visible geometric albedo when ground-based visible-light measurements are available. Previous works (Nugent et al. 2015, 2016; Masiero et al. 2017, 2020) have presented the results of thermal model fitting for NEOs and main belt asteroids (MBAs) observed in the first 5 yr of the NEOWISE reactivation. In this paper, we present results from Years 6 and 7 of the NEOWISE Reactivation survey. We also discuss some of the characteristics of the population of MBAs discovered by NEOWISE during Reactivation, as the extent of this population was somewhat unexpected. Although NEOWISE's sensitivity to objects in the main belt is greatly diminished compared to the Cryogenic mission, its unique field of regard among asteroid surveys means that it is more sensitive to different subpopulations.

2. Observations

The NEOWISE survey pattern is fixed by the spacecraft's orbital geometry. Originally launched on an orbit perpendicular to the Earth–Sun line, the slight atmospheric drag over the course of the mission has reduced the spacecraft's altitude and caused the orbit to precess, shifting NEOWISE's orbital plane by $\sim 20^\circ$. On the side of increasing solar elongation survey observations continue to be made in a zenith-pointing direction (to reduce the thermal load on the telescope), while on the side of decreasing elongation the survey observations continue to point perpendicular to the Sun (due to the constraints on

⁶ <https://irsa.ipac.caltech.edu>



Original content from this work may be used under the terms of the [Creative Commons Attribution 4.0 licence](https://creativecommons.org/licenses/by/4.0/). Any further distribution of this work must maintain attribution to the author(s) and the title of the work, journal citation and DOI.

pointing set by the Sun shield) at the cost of an increased heat load on the telescope from Earth.

The detector performance has remained remarkably stable over the course of the increased heating associated with orbital precession. The telescope’s cryostat acts as an insulator modulating the changes in temperature over each orbit, though overall seasonal changes in telescope temperature are observed following the precession of the orbit. These result in decreases to sensitivity at the <0.02 mag level for W2 during the warmest phases of the orbit (see Sec I.2.c.iii, Figure 11, and Sec IV.2.d.ii of Cutri et al. 2015). Otherwise, NEOWISE’s recent performance has remained consistent with that of previous survey phases.

NEOWISE scans an arc of sky each half-orbit. Every 11 s, the two active 1024×1024 pixel HgCdTe detectors capture an image of a $47' \times 47'$ area of sky simultaneously at 3.4 and $4.6 \mu\text{m}$ (hereafter W1 and W2). Each image has a $\sim 10\%$ overlap with the previous image along the scan direction. Source detection and photometry are performed on each calibrated image, providing a list of sources that are searched for candidate moving objects. The mission uses the WISE Moving Object Processing System (WMOPS; Mainzer et al. 2011a) to perform a blind search for solar system objects. All candidate moving objects detected at least five times and vetted to be real by automatic and human quality assurance are reported to the Minor Planet Center (MPC)⁷ for publication and archiving. The MPC associates observations with known objects, or assigns designations for newly discovered ones, as well as calculating orbits for all minor planets.

The analysis presented here covers data obtained during the survey’s sixth and seventh years (2018 December 13 to 2019 December 12, and 2019 December 13 to 2020 December 12). The NEOWISE Explanatory Supplement (Cutri et al. 2015), which is updated for each data release, provides further details about the mission parameters, data calibration, and data access. To extract data from the archive, we follow the methodology described in previous NEOWISE-related publications (e.g., Masiero et al. 2017). Physical properties from previous publications are archived on the NASA Planetary Data System (Mainzer 2019), and the fits presented here will be added to that archive at a future update.

3. Thermal Modeling Technique

Asteroids absorb incident sunlight, are warmed by it, and then reemit that energy as thermal emission. When the orbit of an object is sufficiently well known, the solar flux it receives at any given time is precisely constrained, and so a representational model can be used to determine how the incident energy would be processed and emitted as thermal radiation. By comparing the modeled flux to the measured infrared flux, we can determine the size of the model that best reproduces the measurements and therefore constrains the size of the asteroid. When rotation rates, rotation poles, and 3D asteroid shape models are available along with multiple epochs of infrared data, detailed thermophysical models can be used to precisely constrain the dimensions and thermal inertia of the body (e.g., Alí-Lagoa et al. 2014; Koren et al. 2015; Yu et al. 2017; Hanuš et al. 2018). When resolved images and in situ thermal measurements are available, maps of thermal inertia across the surface can even be measured (Rozitis et al. 2020).

For the majority of objects observed by NEOWISE, little is known beyond their orbit and a constraint on the absolute visible magnitude H_V . Therefore, we employ a simplified model to analyze their thermal emission known as the Near-Earth Asteroid Thermal Model (NEATM; Harris 1998). NEATM assumes that the asteroid is a sphere, with zero thermal emission contributed from the night side of the body. In this way, we can constrain the size of a sphere that best fits the observed thermal flux and determine a spherical-equivalent diameter for the body. Real asteroids are not spheres, though, so there is some inherent model uncertainty from the shape of the body. In addition, observations at larger solar phase angles will see larger fractions of the night side, increasing model deviation from the actual size in a systematic way (see Mommert et al. 2018, for a discussion on these uncertainties). In contrast, as heliocentric distance and phase angle are coupled for NEOWISE owing to the survey pattern (with higher phase objects will be closer to the Sun and warmer), the thermal emission for high-phase objects will peak closer to the W2 bandpass, which can result in smaller calculated statistical uncertainties from the unknown beaming parameter.

NEATM employs a wavelength-independent variable η , known as the beaming parameter, to allow the model to be adjusted to account for the differences between the modeling assumptions and the actual thermophysical properties of the surface (Harris 1998). This is a simplification of actual asteroidal surfaces that can show emissivity changes as a function of wavelength of order 10% (Salisbury & Walter 1989). The η parameter is dependent on phase (e.g., Spencer et al. 1989; Delbo’ et al. 2007; Harris et al. 2007; Mainzer et al. 2011b), though the η -phase relation shows significant scatter due to a combination of the specific observing conditions of the object and the thermophysical properties of the surface (Harris & Drube 2014, 2020). Following previous work (Masiero et al. 2020), the beaming parameter was held fixed for all fits, as the majority of cases have only a single thermally dominated band (W2). That work found that for the few cases that do have significant thermal emission in W1, the reflected contribution to W1 is not well-enough known to enable a strong constraint on the contribution of emission versus reflection, leading to highly uncertain fits. For the purposes of our modeling, we assume $\eta = 1.4 \pm 0.5$ for NEOs (Mainzer et al. 2011b), while for MBAs we assume $\eta = 0.95 \pm 0.2$ (Masiero et al. 2011). The uncertainty on η is included in our Monte Carlo analysis to propagate to the final uncertainty on the fitted parameters: diameter and albedo. This uncertainty on assumed η is significantly larger than the change in expected η across the phase angles our NEOs are observed at, and thus it accounts for any offset due to this relationship.

Following the methods used for previous analyses of NEOWISE data (most recently Masiero et al. 2020), we use the NEOWISE positions and observation times reported to and archived by the MPC as the starting point for our data extraction. This ensures that observations have been vetted both by the NEOWISE mission during processing and reporting and by the MPC during ingest. We used all observations in the time period of Years 6 and 7 with the C51 observatory code assigned to NEOWISE. These detections, along with the associated spacecraft positions, were extracted from the MPC’s observation file and used as input for a query of the NEOWISE Single-Exposure database hosted by IRSA to retrieve the photometry associated with each detection.

⁷ <https://www.minorplanetcenter.net>

The database was searched for detections that matched the MPC-archived observations to within $5''$ in position and 5 s in time.

The observations extracted from the NEOWISE database were filtered based on the quality of the point-spread function (PSF) fit to the W2 band. We focus on W2 for this quality cut because this band dominates the thermal fit for NEOs and MBAs, and noise in this measurement can result in large changes to the reported diameter. We remove all detections from consideration for fitting that have $w2rchi2 > 5$, which is the reduced χ^2 of the goodness of fit of the PSF to the source profile in the W2 band. This typically is a result of a cosmic-ray strike coincident with the detection, which would cause a dramatic increase in the photometry and thus an overestimate of diameter. Additionally, we remove any objects from consideration for fitting that have orbital arcs of less than 0.02 yr, indicating that these objects have not received sufficient follow-up to have a well-constrained orbit. Without a good orbit, the geocentric distance becomes underconstrained, which has a negative impact on the quality of the diameter fit.

We also exclude detections that were coincident within the same search radius with a stationary background object. Background sources were identified from the stacked Atlas catalog from the 2010 cryogenic WISE survey data⁸ (Cutri et al. 2012). Sources were only removed if $W2 - W2_{\text{atlas}} > -1$ mag to ensure that faint background objects would not remove valid detections of bright asteroids. This rejection of background-contaminated sources occurred for 2.9% of sources in each survey year.

Our implementation of NEATM uses a sphere made of 288 facets, with the temperature on each facet and the flux observed from each facet determined based on the observational geometry. We color-correct the flux from each facet based on its blackbody temperature following Wright et al. (2010), with corrections ranging from 1.005 for reflected light to 1.1–1.5 for emission from subsolar facets (with cooler facets having much larger corrections but significantly smaller contributions to the total flux). The total modeled flux is then compared to the measured flux, and the variable parameters diameter (D) and visible geometric albedo (p_V) are found through the least-squares optimization routine in the *scipy* package (Virtanen et al. 2020). To reduce diameter bias due to the unknown shape and rotation phase at the time of observation, we require a minimum of three detections with W2 photometric uncertainties $w2sigmpro < 0.25$ mag, which are fit simultaneously with a single spherical model. It should be noted that to be identified as a candidate by the WMOPS system an object must be detected at least five times, so the three-detection minimum would only reject objects for cases where a cosmic ray or nearby star spoiled multiple detections. This only occurred for 8 NEOs and 75 MBAs across both years of data.

To constrain the albedo, we require an external measurement of the visible brightness of the body. For this work, we use the published absolute visible magnitude (H_V) included in the MPC orbital catalog, which is calculated by the MPC (along with the G_V slope parameter) based on all submitted photometry after conversion to V band. The uncertainty on H_V is a primary component of the uncertainty on the derived albedo for NEOs (see Masiero et al. 2021, for a discussion of this uncertainty),

along with the uncertainty on diameter from the unknown beaming parameter value, which is often the dominant component in these cases. However, uncertainty measurements are not included with the MPC's H_V values, and so they must be assumed for the vast majority of objects we fit here. Previous research (e.g., Pravec et al. 2012; Vereš et al. 2015) has highlighted systematic biases in the MPC H_V magnitude values for subsets of the data. Following previous work (e.g., Masiero et al. 2020), we update our H_V magnitudes to the improved values from Vereš et al. (2015) and assume an uncertainty of 0.2 mag on the H_V for NEOs and 0.05 mag for MBAs, as these tend to have a significant number of archived visible-light observations. To model the reflected light component, we assume that the G_V slope parameter has an uncertainty of 0.1 and that the ratio of albedos in the infrared to the visible is $p_{IR}/p_V = 1.6 \pm 1.0$ for NEOs and $p_{IR}/p_V = 1.5 \pm 0.5$ for MBAs following previous analyses (Mainzer et al. 2011b; Masiero et al. 2011). Once formal uncertainties are available for absolute magnitude measurements for the majority of asteroids, characterization of the uncertainty on albedo will improve somewhat.

The diameter constraints determined by fitting NEATM models to the NEOWISE data are only valid for cases where at least one band is dominated by thermal emission. As noted in previous work (e.g., Masiero et al. 2020), due to the uncertainty on the ratio of IR to visible albedos, NEATM fits with reflected light contributions $> 10\%$ enter a regime where the model becomes underconstrained and highly uncertain. We check the reflected light contribution in each band for every fit and remove any with $> 10\%$ reflected light contribution to W2. This resulted in the removal of 29% of MBAs in both years, 8% of NEOs observed in Year 6, and 13% of NEOs observed in Year 7. A detailed description of the reflected light model can be found in Mainzer et al. (2011d).

To assess the statistical uncertainty on the resulting diameter and albedo fits, we perform Monte Carlo trials using the uncertainties on the measured NEOWISE and H_V magnitudes, as well as the defined variation ranges on the assumed parameters (η , p_{IR}/p_V). We perform 25 trials, with each trial drawing a different measured or assumed parameter using a normal distribution with the initial value as the mean and the uncertainty as the width. The standard deviation of the output fitted values (D and p_V) is taken as the statistical uncertainty for the fit of those values. There are additional systematic uncertainties inherent to our fitting method that will also affect our results, which we discuss below.

4. Results

We present the results of our diameter and albedo fitting in tables below. The NEOs and MBAs observed in Year 6 are given in Tables 1 and 2, respectively, while the NEO and MBA fits from Year 7 are given in Tables 3 and 4, respectively. The Year 6 table contains physical property measurements for 199 NEOs and 5851 MBAs, while the Year 7 table contains 175 NEOs and 5861 MBAs. Each table lists the MPC-packed designation for the object, the H_V and G_V absolute magnitude and slope parameters that were used as input measurements for the fits, the diameter and albedo with associated statistical errors, the number of detections in the W1 and W2 bands used for the fit, and the phase angle at the midpoint of observation. Fitted albedos are presented with asymmetric error bars, as the uncertainties are derived from magnitude uncertainties, which

⁸ <https://irsa.ipac.caltech.edu/cgi-bin/Gator/nph-scan?mission=irsa&submit=Select&projshort=WISE>

Table 1
Thermal Model Fits for NEOs Detected in the Sixth Year of the NEOWISE Survey

Name	H^a (mag)	G	Diameter (km)	p_V^b	Beaming	n_{W1}	n_{W2}	Phase (deg)
02059	15.90	0.15	1.84 ± 0.79	$0.179 (+0.188/-0.092)$	1.40 ± 0.50	20	20	46.50
02100	16.30	0.15	2.05 ± 0.83	$0.126 (+0.123/-0.062)$	1.40 ± 0.50	0	5	58.48
02100	16.30	0.15	1.46 ± 0.52	$0.251 (+0.263/-0.128)$	1.40 ± 0.50	0	13	66.45
03102	16.20	0.15	1.80 ± 0.64	$0.241 (+0.213/-0.113)$	1.40 ± 0.50	23	25	53.37
03200	14.30	0.15	2.95 ± 1.12	$0.194 (+0.182/-0.094)$	1.40 ± 0.50	7	7	46.02
03552	12.90	0.15	49.02 ± 31.66	$0.005 (+0.009/-0.003)$	1.40 ± 0.50	0	12	18.79
04487	17.30	0.15	1.24 ± 0.41	$0.138 (+0.181/-0.078)$	1.40 ± 0.50	0	12	51.96
05189	17.80	0.15	0.55 ± 0.17	$0.448 (+0.323/-0.188)$	1.40 ± 0.50	0	4	69.10
05626	14.20	0.15	4.78 ± 1.99	$0.181 (+0.182/-0.091)$	1.40 ± 0.50	21	23	52.08
06178	15.80	0.15	4.22 ± 1.77	$0.047 (+0.071/-0.028)$	1.40 ± 0.50	0	13	41.18

Notes.

^a Measured H used as input for the modeling; the model-output H value can be found using the output diameter, albedo, and the equation $D = 1329 \times 10^{H/-5} / \sqrt{p_V}$.

^b Albedo uncertainties are symmetric in log-space owing to the uncertainty on H ; the asymmetric linear equivalents of the 1σ log-space uncertainties are presented here.

(This table is available in its entirety in machine-readable form.)

Table 2
Thermal Model Fits for MBAs Detected in the Sixth Year of the NEOWISE Survey

Name	H^a (mag)	G	Diameter (km)	p_V^b	Beaming	n_{W1}	n_{W2}	Phase (deg)
00021	7.50	0.15	108.04 ± 28.59	$0.131 (+0.079/-0.049)$	0.95 ± 0.20	6	6	24.75
00034	8.60	0.15	116.91 ± 35.99	$0.036 (+0.054/-0.021)$	0.95 ± 0.20	12	8	20.48
00036	8.60	0.15	106.25 ± 25.32	$0.047 (+0.029/-0.018)$	0.95 ± 0.20	13	13	24.83
00038	8.50	0.15	86.66 ± 23.47	$0.094 (+0.058/-0.036)$	0.95 ± 0.20	0	10	23.05
00045	7.50	0.15	230.72 ± 89.48	$0.033 (+0.051/-0.020)$	0.95 ± 0.20	0	7	20.30
00045	7.50	0.15	220.00 ± 63.65	$0.041 (+0.027/-0.016)$	0.95 ± 0.20	12	10	23.24
00046	8.50	0.15	132.76 ± 60.42	$0.042 (+0.047/-0.022)$	0.95 ± 0.20	10	10	20.55
00046	8.50	0.15	116.80 ± 39.19	$0.047 (+0.037/-0.021)$	0.95 ± 0.20	12	10	24.06
00051	7.60	0.15	138.85 ± 36.79	$0.075 (+0.045/-0.028)$	0.95 ± 0.20	10	9	21.78
00051	7.60	0.15	126.55 ± 34.76	$0.088 (+0.057/-0.035)$	0.95 ± 0.20	14	15	24.85

Notes.

^a Measured H used as input for the modeling; the model-output H value can be found using the output diameter, albedo, and the equation $D = 1329 \times 10^{H/-5} / \sqrt{p_V}$.

^b Albedo uncertainties are symmetric in log-space owing to the uncertainty on H ; the asymmetric linear equivalents of the 1σ log-space uncertainties are presented here.

(This table is available in its entirety in machine-readable form.)

Table 3
Thermal Model Fits for NEOs Detected in the Seventh Year of the NEOWISE Survey

Name	H^a (mag)	G	Diameter (km)	p_V^b	Beaming	n_{W1}	n_{W2}	Phase (deg)
00887	13.78	0.15	6.62 ± 2.04	$0.124 (+0.151/-0.068)$	1.40 ± 0.50	10	9	37.41
01685	14.31	0.15	2.61 ± 0.72	$0.395 (+0.247/-0.152)$	1.40 ± 0.50	12	13	70.62
02102	16.01	0.15	1.43 ± 0.52	$0.308 (+0.267/-0.143)$	1.40 ± 0.50	9	9	52.93
03360	15.91	0.15	2.70 ± 1.01	$0.138 (+0.123/-0.065)$	1.40 ± 0.50	5	5	56.89
03360	15.91	0.15	3.17 ± 1.76	$0.076 (+0.155/-0.051)$	1.40 ± 0.50	0	10	35.06
04055	14.71	0.15	2.61 ± 1.03	$0.335 (+0.317/-0.163)$	1.40 ± 0.50	37	38	55.59
04953	14.99	0.15	2.73 ± 1.00	$0.228 (+0.197/-0.106)$	1.40 ± 0.50	5	6	50.56
07753	17.96	0.15	1.64 ± 0.71	$0.043 (+0.075/-0.027)$	1.40 ± 0.50	0	10	39.21
08014	18.90	0.15	0.34 ± 0.11	$0.433 (+0.339/-0.190)$	1.40 ± 0.50	0	6	75.94
09172	16.32	0.15	3.88 ± 1.87	$0.035 (+0.088/-0.025)$	1.40 ± 0.50	0	6	38.96

Notes.

^a Measured H used as input for the modeling; the model-output H value can be found using the output diameter, albedo, and the equation $D = 1329 \times 10^{H/-5} / \sqrt{p_V}$.

^b Albedo uncertainties are symmetric in log-space owing to the uncertainty on H ; the asymmetric linear equivalents of the 1σ log-space uncertainties are presented here.

(This table is available in its entirety in machine-readable form.)

Table 4
Thermal Model Fits for MBAs Detected in the Seventh Year of the NEOWISE Survey

Name	H^a (mag)	G	Diameter (km)	p_V^b	Beaming	n_{W1}	n_{W2}	Phase (deg)
00013	6.79	0.15	228.76 ± 71.61	$0.043 (+0.043/-0.021)$	0.95 ± 0.20	7	8	24.22
00034	8.63	0.15	100.60 ± 29.01	$0.042 (+0.045/-0.022)$	0.95 ± 0.20	8	7	20.59
00038	8.54	0.15	113.40 ± 37.72	$0.044 (+0.036/-0.020)$	0.95 ± 0.20	15	14	22.20
00049	7.84	0.15	151.38 ± 42.01	$0.041 (+0.040/-0.020)$	0.95 ± 0.20	9	7	21.73
00049	7.84	0.15	138.89 ± 46.07	$0.049 (+0.038/-0.021)$	0.95 ± 0.20	26	24	21.96
00056	8.52	0.15	130.75 ± 28.65	$0.040 (+0.020/-0.013)$	0.95 ± 0.20	11	15	27.27
00058	9.04	0.15	87.34 ± 27.34	$0.045 (+0.037/-0.020)$	0.95 ± 0.20	11	10	21.09
00058	9.04	0.15	93.52 ± 30.99	$0.039 (+0.030/-0.017)$	0.95 ± 0.20	5	5	22.38
00066	9.54	0.15	67.89 ± 27.57	$0.042 (+0.056/-0.024)$	0.95 ± 0.20	19	20	19.30
00072	9.10	0.15	68.27 ± 18.68	$0.091 (+0.069/-0.039)$	0.95 ± 0.20	12	11	24.37

Notes.

^a Measured H used as input for the modeling; the model-output H value can be found using the output diameter, albedo, and the equation $D = 1329 \times 10^{H/-5} / \sqrt{p_V}$.

^b Albedo uncertainties are symmetric in log-space owing to the uncertainty on H ; the asymmetric linear equivalents of the 1σ log-space uncertainties are presented here.

(This table is available in its entirety in machine-readable form.)

are symmetric in log-space, and to ensure that the low-albedo objects with poorly constrained H_V values will not have albedo measurements smaller than the 1σ uncertainty. Figure 1 shows the diameter and albedo fits for all NEOs observed during the first seven years of the Reactivation survey, combining these results with those from previous publications (Mainzer 2019; Masiero et al. 2020).

Combining the model-output diameter and albedo values will allow for the determination of the “best-fit” H_V that resulted from the joint emitted light/reflected light model. In cases where W1 is dominated by reflection, the reflected light component is fit simultaneously to both the measured W1 and predicted V fluxes based on the input H_V and G_V . If the uncertainty on the W1 measurement is smaller than the uncertainty on H_V (which is often the case), this will result in the model fit favoring W1 and the output H_V deviating from the input H_V within the uncertainty. These differences show systematic offsets at the ~ 0.2 mag level because (1) the p_{IR}/p_V ratio depends on the composition of asteroids (Mainzer et al. 2011c), while we assume a single median value for the whole population; (2) our removal of objects with significant reflected light in W2 preferentially removes high-albedo objects like S-types (Masiero et al. 2017) from the main belt data set, skewing the expected albedo ratio; and (3) the MPC’s H_V determinations are known to have systematic offsets (Pravec et al. 2012; Vereš et al. 2015).

Objects will appear multiple times within a single results table when they have been seen at multiple different epochs within that year. When the orbital and viewing geometries are sufficiently different between observations, a simple NEATM fit cannot be used across epochs owing to changes in subsolar temperature and phase angle, so these objects are presented as separate entries for each epoch. Differences in fitted diameter between epochs are a combination of the changing viewing aspect of the nonspherical body (and thus change to the effective spherical diameter fit to the projected shape) and statistical and model uncertainties. When multiple epochs are available, along with ancillary data such as rotation period and pole, more advanced thermophysical modeling can provide insights into the 3D shape and thermophysical properties of the

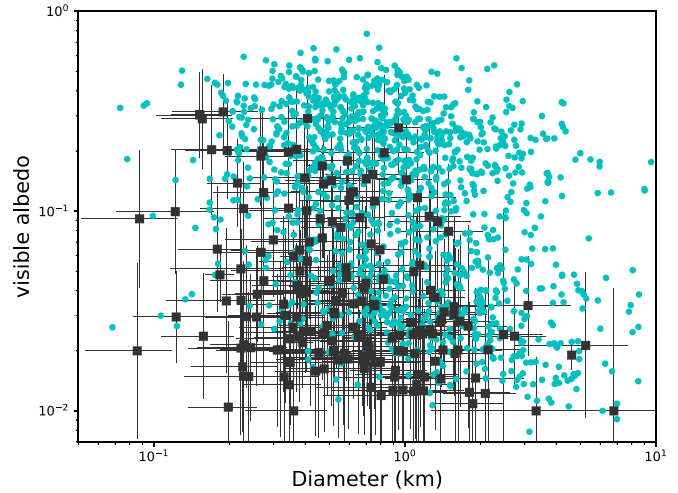


Figure 1. Diameters derived from thermal modeling compared to geometric visible albedos for all objects observed by NEOWISE (cyan circles) and those discovered by NEOWISE (black squares) during the first seven years of the Reactivation mission. Objects discovered by NEOWISE tend to be lower albedo and larger than a few hundred meters, occupying a niche that other surveys are less successful at detecting. Uncertainties are only shown for discovered objects for clarity, but they are comparable in size for the previously known asteroids.

surface (see, e.g., Koren et al. 2015; Hanuš et al. 2016, 2018; Masiero et al. 2019). Large differences between the fits from different epochs presented here indicate objects that would likely benefit from more advanced modeling.

One object in the Year 6 NEO list has an anomalously low albedo ($p_V = 0.005$) and a very large diameter ($D = 49 \pm 32$ km), even after filtering of the data and verification of the detections. This object, (3552) Don Quixote, has a 6.665 hr period and a light-curve amplitude that can be as large as 1.24 mag (Warner et al. 2019), indicating that it is highly elongated. The half-period of this object’s rotation is nearly the same as the ~ 188 -minute period between NEOWISE observations, as determined by the orbit and survey plan, meaning that we expect significant aliasing in the observations. If NEOWISE detected this object near a light-curve maximum, we would expect all observations from that epoch to be near the maximum, resulting in a size constraint that

reflects only the longest axis. Using an H_V value derived from all rotation phases would then result in an anomalously low albedo.

Alternately, Don Quixote is known to be an active, cometary object (Mommert et al. 2014), and emission of gas and dust will cause the measured flux in W1 and W2 to be increased above what would be expected for the bare nucleus. Emission from CO and CO₂ in particular can cause significant flux excesses in the W2 band (e.g., Bauer et al. 2015). While our images show no discernible coma or tail, recent observations of Don Quixote have shown that it experienced cometary outgassing approximately 6 months before the NEOWISE observations (Mommert et al. 2020), and any coma contribution to the observed flux from dust or gas would also result in an increase in the derived size and thus the very low albedo constraint. Our size and albedo constraints derived here for (3552) Don Quixote would be expected to be less reliable than for a typical object, which is reflected in the very large uncertainty on the diameter. (3552) Don Quixote was also observed by NEOWISE in Year 5 of its survey before the onset of the most recent activity, providing a diameter constraint of 27 ± 13 km and an albedo of $0.03^{+0.03}_{-0.02}$ (Masiero et al. 2020), more consistent with other literature values of $D = 19$ km (Chapman et al. 1994) and 18.4 km (Mommert et al. 2014).

Two objects in the Year 7 NEO list also yield anomalously low albedos in our fits: (248590) and 2008 CG119. NEO (248590) has three other epochs of fitted diameters in the NEOWISE data (Mainzer 2019), with reported albedos of $p_V = 3.7\%$, 1.8% , and 1.1% . This, along with the albedo here of $p_V = 0.9\%$, points to a likely incorrect H_V magnitude, which would bias all of the albedos to very low values. Fitting H_V magnitudes suffers from numerous potential sources of error, and so large offsets can occur, especially for NEOs (Masiero et al. 2021). In this case, our assumed uncertainty on the H_V magnitude may also be underestimated. In contrast, 2008 CG119 only had three detections that survived our quality cuts, increasing the chances that rotational light-curve variations would bias the diameter fit upward and thus the albedo downward. In addition, the uncertainty on the diameter fit is large, further complicating interpretation of the albedo.

As discussed above, phase angle is linked to heliocentric distance and thus temperature for NEOWISE, with higher-phase objects being warmer. Given the large range of possible beaming values for NEOs, cooler objects would be expected to show larger statistical diameter uncertainties, as the peak flux will be further from the bandpass. This is shown in Figure 2, where the NEOs at phases below $\alpha = 40^\circ$ show increased statistical diameter uncertainty. This is the opposite behavior to what would be expected for the systematic uncertainty, as described by Mommert et al. (2018). Systematic uncertainty components must be derived on a population level by comparison with other diameter data sets (as described in the next section).

5. Discussion

5.1. Diameter Accuracy

The accuracy of the diameter fits from the NEOWISE Reactivation survey has been highly stable over the lifetime of the mission (see Masiero et al. 2020). This is not surprising given that the photometric performance of the system has been nearly unchanged since launch (Cutri et al. 2015) and the thermal modeling methodology has also remained unchanged. Previous

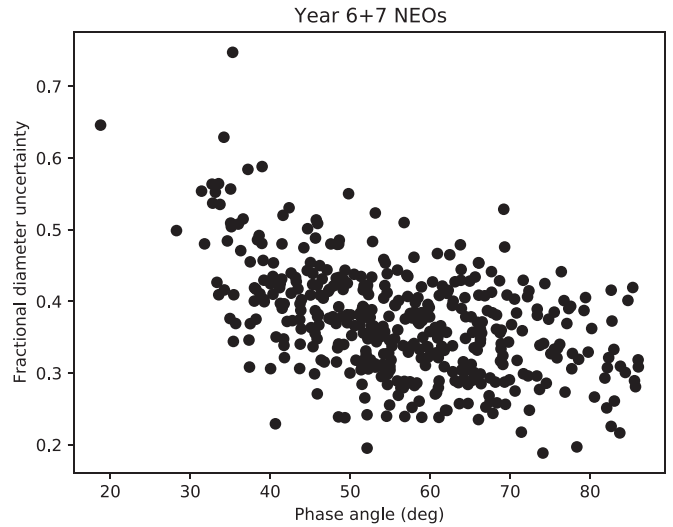


Figure 2. Fractional diameter uncertainty (σ_D/D) for all NEO measurements in NEOWISE Years 6 and 7 vs. phase angle. The uncertainty shown here only includes the statistical component determined through our Monte Carlo analysis. Objects at smaller phase angles show larger fractional uncertainties because the peak of thermal emission is further from the W2 bandpass, providing a weaker constraint on the size given the large range of possible beaming values.

works have demonstrated this primarily through comparison of diameter fits for MBAs due to the much larger number of MBAs observed by the mission. This is because MBAs are more numerous and because the synodic periods of NEOs are longer, and so opportunities to reobserve them are less frequent.

However, now that NEOWISE has been operating in its Reactivation mission for over 7 yr, we have a sufficiently large sample of observed NEOs that also have literature diameter measurements from the cryogenic NEOWISE mission, as well as a smaller set with diameter constraints independent of thermal infrared models such as asteroid radar echoes or occultations. Comparisons between the Reactivation data and the cryogenic NEOWISE diameters allow us to determine the effect on the fits of only fitting the Wien's side of the blackbody emission spectrum (compared to fitting near the peak of the spectrum with the cryogenic data), while comparison with non-IR diameters allows us to assess the accuracy of the overall NEATM method.

NEOWISE has observed 83 unique NEOs at 182 epochs during the first seven years of Reactivation that also have diameter fits from the cryogenic phase of the NEOWISE mission (Mainzer et al. 2011b). The comparison between the cryo fits and the Reactivation fits is shown in Figure 3. The best-fit Gaussian to the fractional diameter differences (Reactivation diameter minus the cryo diameter divided by the cryo diameter) indicates that there is a slight systematic offset between the data sets of 4%, with the cryo diameters being larger. The 1σ scatter of 31% is attributed to a combination of the different viewing geometries presenting different projections of the profile, as well as the need to assume a beaming parameter for all of the Reactivation fits.

We also compare our Reactivation NEO fits to the spherical-equivalent diameters derived from 3D modeling of radar echoes of NEOs obtained at the Arecibo and Goldstone facilities (Benner et al. 2015), as shown in Figure 4. Radar diameters are obtained from a set of publications presenting individual or collections of fits (Hudson & Ostro 1995, 1999; Benner et al. 1999; Shepard et al. 2006; Busch et al. 2007, 2008;

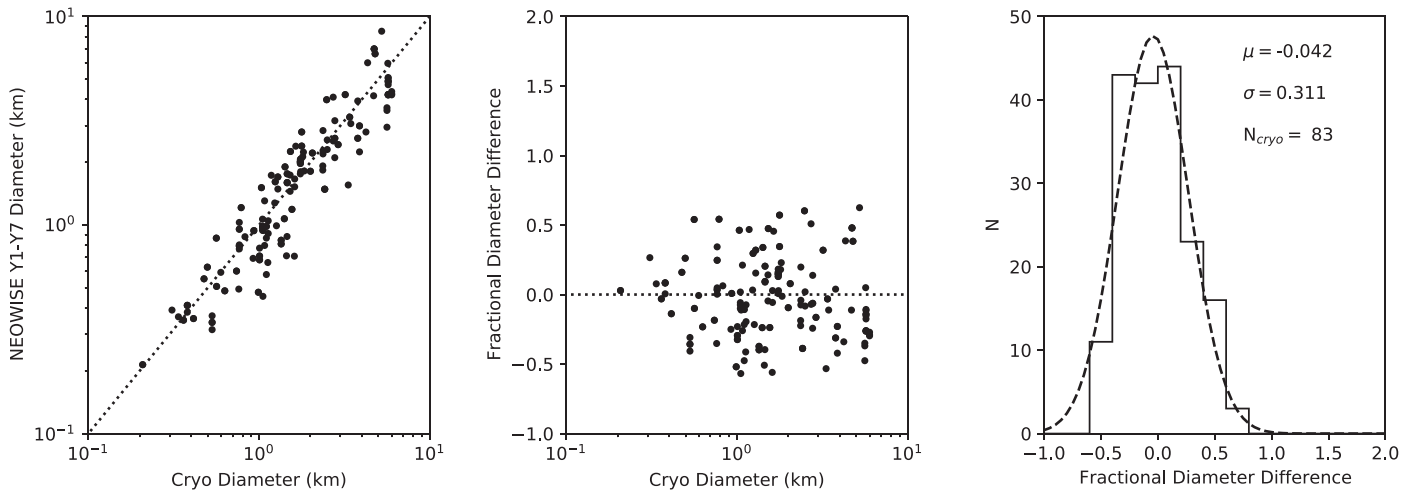


Figure 3. Diameters of NEOs observed during the first seven years of Reactivation compared to the diameter fits based on cryogenic NEOWISE data (left panel, with the dotted line indicating a one-to-one relationship). The middle panel shows the fractional diameter difference of the fits compared to the cryogenic diameters, while the right panel shows a histogram of the fractional diameter differences, as well as a best-fit Gaussian distribution to the histogram (dashed line, with the Gaussian mean (μ) and standard deviation (σ) given).

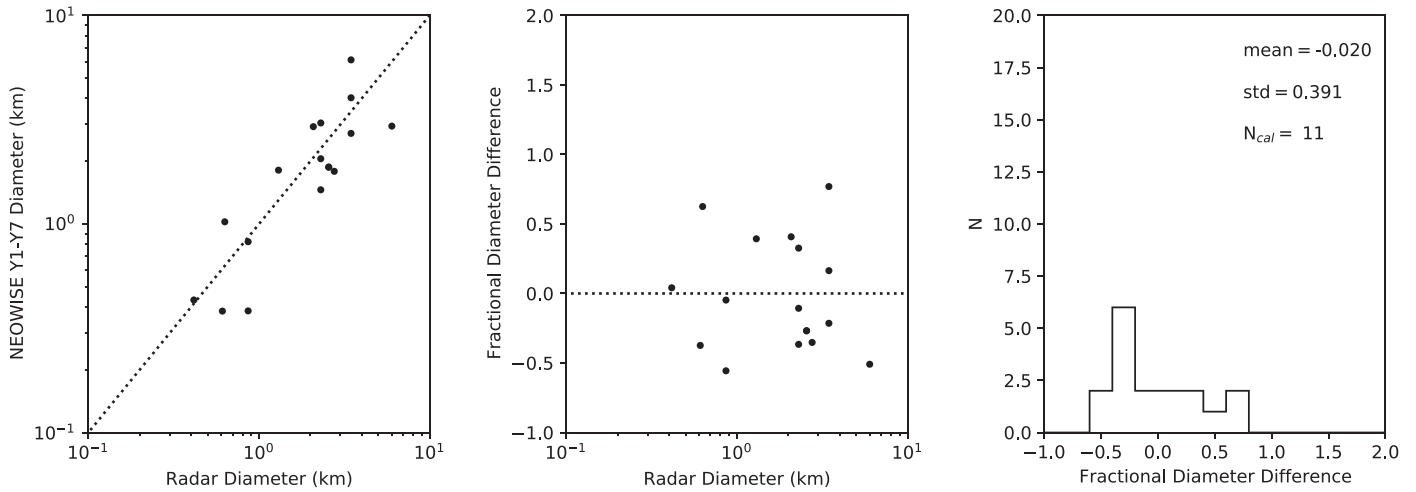


Figure 4. The same as Figure 3, but showing the comparison between diameters from NEOWISE Reactivation and sizes from 3D models of radar observations. Vertical alignments of points in the first two panels are due to individual NEOs observed at multiple NEOWISE epochs. As there are insufficient data for a reliable Gaussian fit, we instead present the mean and standard deviation of the fractional diameter difference distribution.

Jimenez et al. 2010; Magri et al. 2011; Naidu et al. 2015; Taylor et al. 2019; Lawrence & Benner 2020). Because of the difficulty in obtaining sufficiently high signal-to-noise ratio radar observations to allow for 3D modeling, there are only 11 NEOs in the overlap between the two data sets ((1620) Geographos, (2063) Bacchus, (2100) Ra-Shalom, (3200) Phaethon, (4179) Toutatis, (8567) 1996 HW1, (29075) 1950 DA, (33342) 1998 WT24, (185851) 2000 DP107, (276049) 2002 CE26, (363067) 2000 CO101), representing 16 epochs of NEOWISE observation. Having a 3D radar model is important, however, as this typically results in a better measurement of the asteroid's shape and spherical-equivalent size. Due to the limited sample size, a Gaussian fit would not be sufficiently constrained, so instead we calculate the mean and standard deviation of the fractional diameter differences. From the limited data we can see that the systematic offset in the sizes is comparable to that seen for the comparison with the cryogenic NEOWISE data, while the scatter is somewhat larger ($\sim 39\%$). This may be a result of the combination of the effects described above, as well as the

differences between the NEATM model and the radar modeling techniques, which are 10%–15% when the beaming parameter can be fitted to multiple infrared wavelengths (Mainzer et al. 2011d), or may be simply due to small number statistics. As NEOWISE continues to collect data and more radar shape models are published, the sample size should improve and allow for better determination of the differences between model results.

5.2. Objects in the Main Belt Discovered by NEOWISE during Reactivation

As an infrared survey, the detection efficiency of NEOWISE is a function of the temperature of the object. Objects closer to the Sun, and thus warmer, will be significantly brighter than an object of similar size farther from the Sun even after correcting for $\frac{1}{r^2}$ distance effects. Thus, the 40 cm diameter primary mirror used by NEOWISE has comparable sensitivity to much larger visible-light telescopes on the ground when it comes to detecting asteroids and comets near Earth.

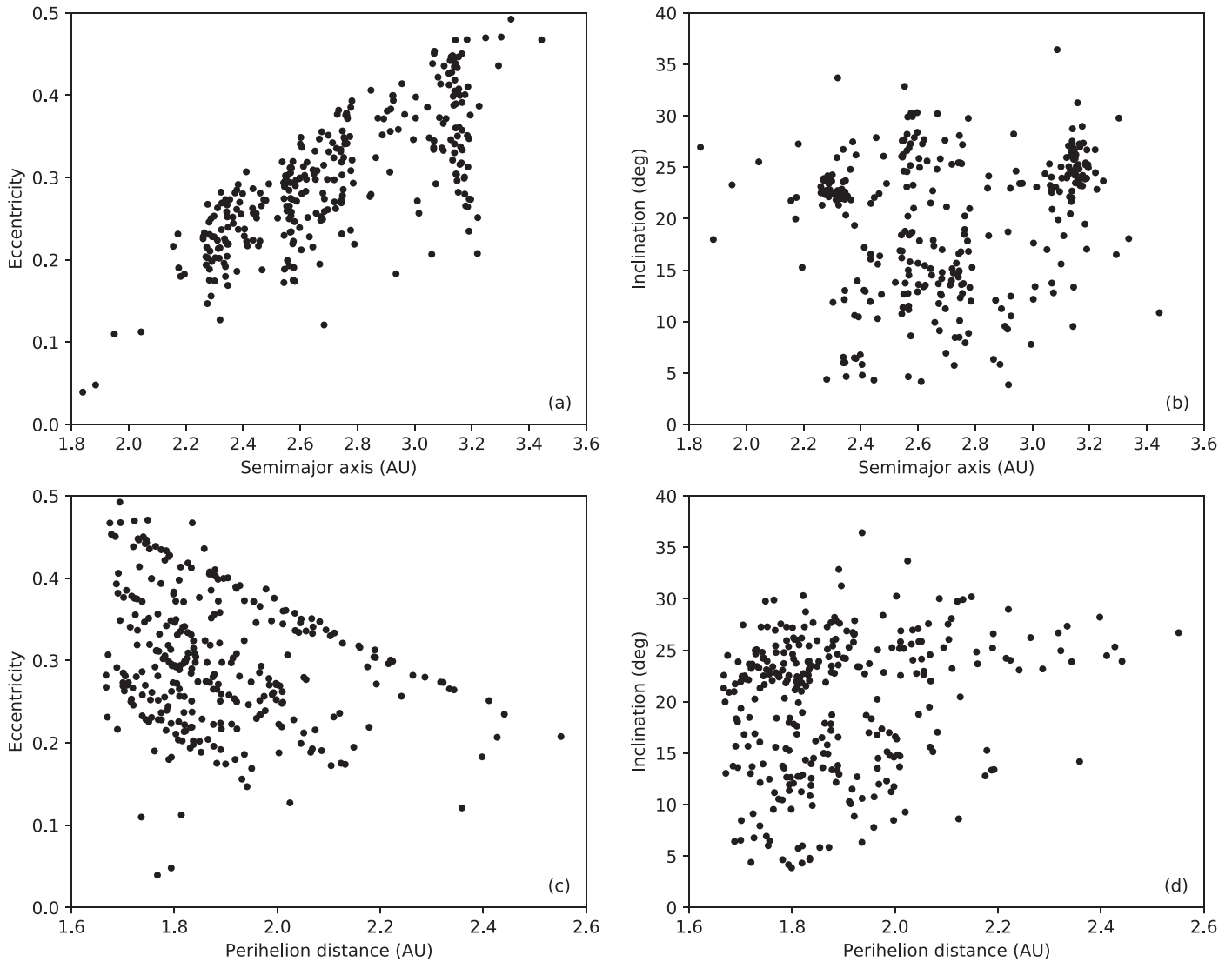


Figure 5. Comparison of the semimajor axes, perihelion distances, eccentricities, and inclinations of the MBAs discovered by NEOWISE during the Reactivation survey. While the majority of discovered objects have perihelia below 2 au, where they will be warmer and thus easier to detect in the infrared, a subset have larger perihelia but also larger orbital inclinations.

For more distant objects like MBAs the peak of the thermal emission moves to longer wavelengths, decreasing the W2 signal-to-noise ratio, while the W1 signal is almost entirely due to reflected light. For these objects NEOWISE’s sensitivity is comparable to a ground-based visible-light telescope of similar size. While NEOWISE discovered tens of thousands of MBAs during its cryogenic mission (Masiero et al. 2011), after the loss of cryogen we would expect the number of main belt discoveries to be minimal.

Instead, we find that a small number of objects in the main belt are still being discovered by NEOWISE. To investigate these objects, as well as the reason that they were not previously found by other ground-based surveys, we searched the MPC’s Observation Archive⁹ for all NEOWISE observations of MBAs from 2013 onward that received a “*” character, designating a discovery observation for an object. For some objects multiple observations will receive a discovery designation by the MPC, in cases where tracklets from different years were given

provisional designations and then later linked. We take an inclusive view of these when a NEOWISE discovery observation was not the first discovery detection, as these indicate cases where the previous observations resulted in an orbit sufficiently uncertain as to essentially be lost.

We show in Figures 5–7 the relationship between various orbital parameters for the discovered MBAs. Figure 5(c) shows that the majority of the discovered objects have perihelion distances (q) near the cutoff for the Mars-crossing population ($q = 1.66$ au). These objects will come closer to the Sun, have higher surface temperatures, and thus be easier to detect in infrared emission. Some discoveries, however, have larger perihelia, which makes them less likely to be bright in the infrared. These high- q objects tend to have larger inclinations, as shown in Figure 5(d), and tend to be clumped near the locations of the Phocaea and Euphrosyne asteroid families (Masiero et al. 2015; Nesvorný 2015; Novaković et al. 2017).

The reason for these correlations begins to be revealed when we look to the distribution of the angular orbital elements, as

⁹ <https://minorplanetcenter.net/iau/ECS/MPCAT-OBS/MPCAT-OBS.html>

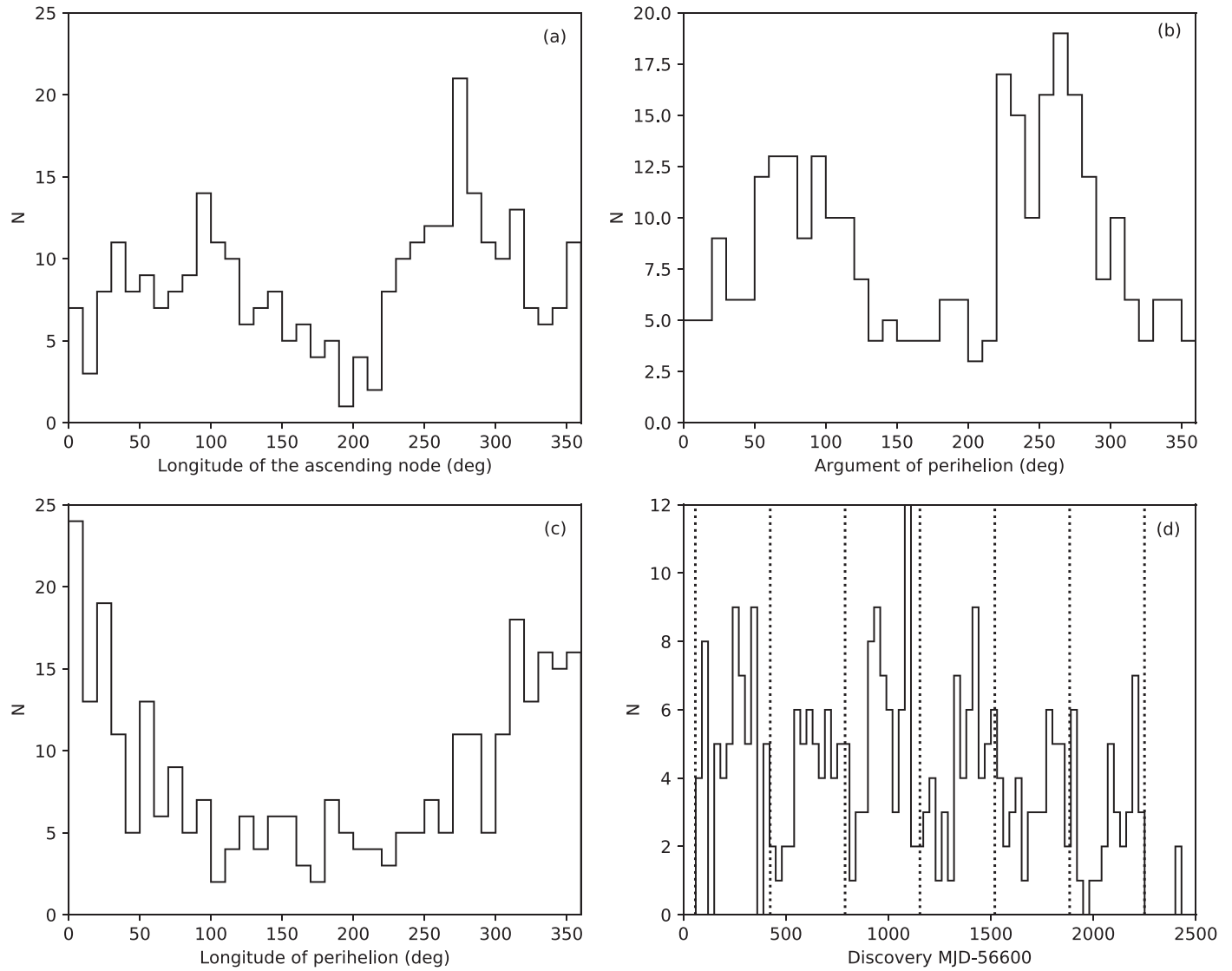


Figure 6. Histograms showing the distribution of angular orbital parameters and discovery dates for all MBAs discovered by NEOWISE during the Reactivation survey. While the distributions of the longitudes of the ascending node and longitudes of perihelion follow the behavior of MBAs in general, the argument of perihelion distribution shows significant differences. Additionally, the date of discovery is skewed toward the summer/fall of each year (each January 1 is shown as the vertical dotted line).

shown in Figure 6. While the structured distribution for the longitude of the ascending node and the sinusoidal distribution for the longitude of perihelion match those seen for the broader main belt population,¹⁰ the argument of perihelion (ω) of the NEOWISE discoveries shows a strong bimodal distribution that is not seen for the overall population, which is flat. The NEOWISE discoveries tend to cluster around $\omega = 90^\circ$ and $\omega = 270^\circ$. Objects with these orbital parameters have their perihelia at their maximum distance above/below the ecliptic. When viewed from Earth, these objects will be at their closest to the Sun when they are far from the celestial equator, where ground-based surveys tend to concentrate.

This is further shown in Figure 7(g), with objects having $\omega = 90^\circ$ and $\omega = 270^\circ$ being discovered at declinations up to $\pm 60^\circ$. Figure 7(b) shows that the clustering in argument of perihelion for the NEOWISE discoveries becomes more pronounced at larger perihelion distances. We interpret this

as indicating that objects missed by ground-based surveys tend to be those that reach their perihelion far off the ecliptic plane.

Another interesting effect is seen in Figure 6(d), which shows that NEOWISE main belt discoveries tend to occur in the later half of the calendar year. We interpret this as resulting from a combination of the ecliptic plane crossing the galactic center near opposition in the summer, the summer monsoon shutdowns experienced by surveys in Arizona, and the shorter nights for ground-based telescopes in the summer. This will cause more objects to be missed at opposition when they would be most visible to ground-based telescopes, allowing them to be picked up a few months later when they enter the NEOWISE scan circle. The overall decrease in discoveries with time is likely a combination of increasing completeness and more recent objects not having had sufficient time to receive incidental follow-up, and thus not appearing in the MPC orbital catalog. The latter cause is particularly apparent in the low number of discoveries from 2020.

¹⁰ <https://minorplanetcenter.net/iau/lists/MPDistribution.html>

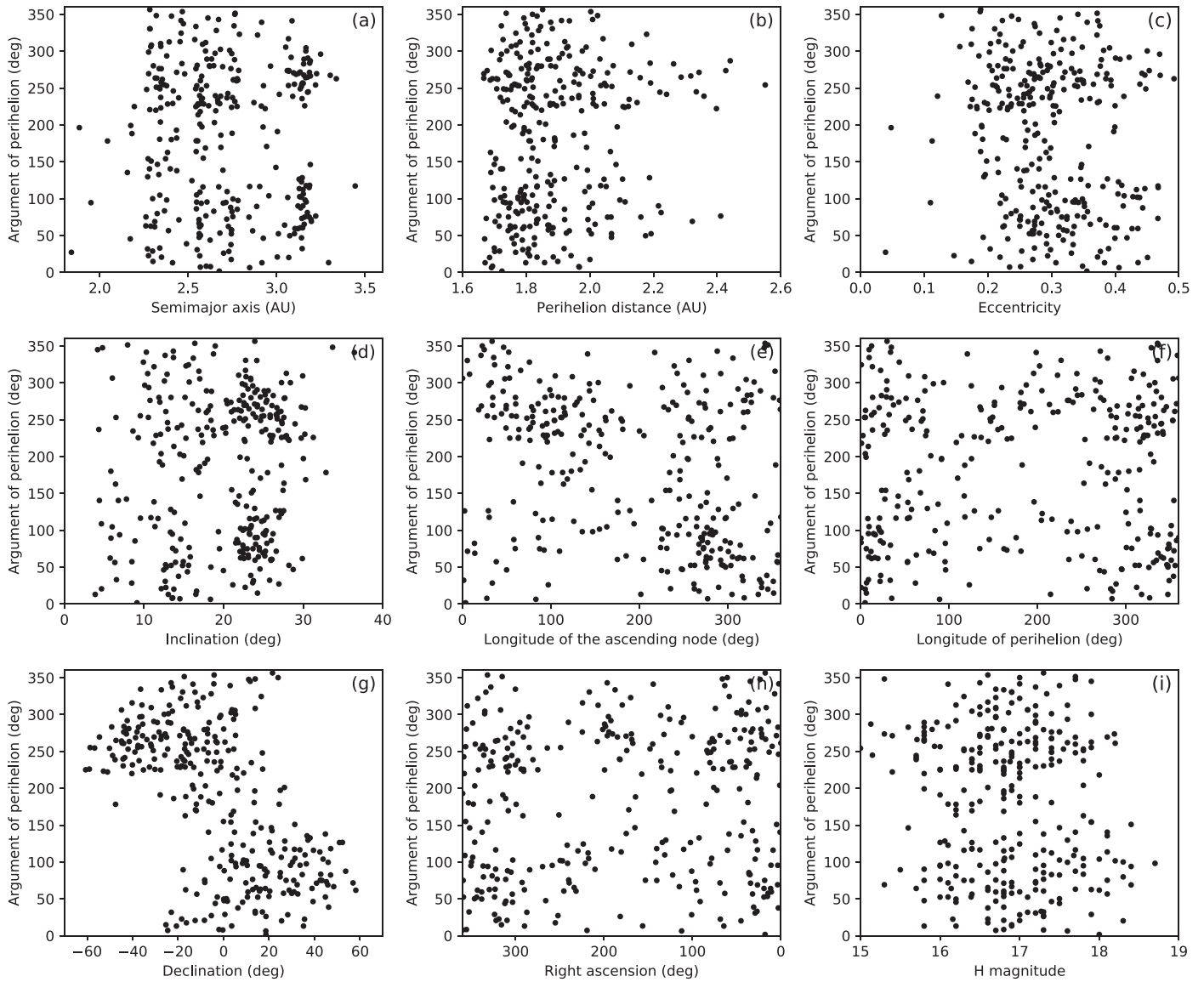


Figure 7. Comparison of the argument of perihelion to different orbital parameters for all MBAs discovered by NEOWISE during the Reactivation mission. Comparisons with perihelion distance (panel (b)) and decl. (panel (g)) show the most significant structure.

6. Conclusions

We present thermal model fits for NEOs and MBAs observed by the NEOWISE mission during the sixth and seventh years of its Reactivated mission (2018 December 13 to 2020 December 12). These include diameter and albedo constraints for 227 epochs of 199 NEOs and 6649 epochs of 5851 MBAs from Year 6 and 197 epochs of 175 NEOs and 6656 epochs of 5861 MBAs from Year 7. When combined with previously published analyses, during its Reactivation mission NEOWISE has provided diameter constraints for 1415 unique NEOs. Including fits from the original cryogenic and post-cryogenic mission data increases this total to 1845 unique NEOs that have been characterized. The NEOs discovered by NEOWISE tend to be low albedo and a few hundred meters in size, a region of phase space that is not well probed by other NEO surveys.

With the larger data set now available, we have compared the NEO diameter fits based on the W1 and W2 bandpasses to those from the cryogenic mission phase that allowed for fitting of the

beaming parameter, as well as to independent diameter determinations from radar observations. We find that needing to assume a beaming parameter when only using data significantly shortward of the thermal peak results in a diameter uncertainty of $\sim 30\%$ when compared to fits using the cryogenic WISE data that span the thermal peak. Comparisons to independent diameter constraints from radar show a larger diameter uncertainty that is consistent with a combination of the need to use a fixed beaming and the deviations of the NEATM model from actual asteroid thermal behavior; however, this is based on the small sample of overlapping objects.

We also investigated the small number of asteroids in the main belt still being discovered by NEOWISE. We show that these objects tend to reside on orbits where their perihelia are significantly out of the ecliptic plane, resulting in detection at high ecliptic latitudes that other surveys do not cover as deeply. There also is a correlation in these discoveries with time of year, which we attribute to a combination of the effects of the ecliptic plane crossing the galaxy in the ground-based surveys' field of regard, as well as monsoon seasonal effects for surveys

in the southwestern United States. For future surveys that probe fainter magnitudes, a highly complete catalog of MBAs will be critical to maximizing the capability to discover new NEOs.

The NEOWISE survey is currently ongoing, even as the spacecraft's orbit continues to precess away from its original terminator-following path. Low levels of solar activity during the last solar minimum resulted in significantly slower orbital evolution, and thus smaller increases in the focal plane temperature than originally anticipated. As the Sun leaves solar minimum and becomes more active, orbital precession is expected to increase, but predictions indicate that the increase in heating will not have an impact on data quality through at least mid-2022. Until such time as the orbital evolution results in significant data degradation, or eventual spacecraft reentry, NEOWISE provides a unique set of measurements of asteroids and comets passing close to Earth and is an important component of Earth's planetary defense ecosystem.

The authors thank the two anonymous referees for their comments, which improved the manuscript. This publication makes use of data products from the Wide-field Infrared Survey Explorer, which is a joint project of the University of California, Los Angeles, and the Jet Propulsion Laboratory/California Institute of Technology, funded by the National Aeronautics and Space Administration. This publication also makes use of data products from NEOWISE, which is a joint project of the University of Arizona and the Jet Propulsion Laboratory/California Institute of Technology, funded by the Planetary Science Division of the National Aeronautics and Space Administration. This research has made use of data and services provided by the International Astronomical Union's Minor Planet Center. This research has made use of the NASA/IPAC Infrared Science Archive, which is funded by the National Aeronautics and Space Administration and operated by the California Institute of Technology. This research has made use of NASA's Astrophysics Data System. This research has made extensive use of the *numpy*, *scipy*, and *matplotlib* Python packages. The authors also acknowledge the efforts of worldwide NEO follow-up observers, both professional and nonprofessional, who provide time-critical astrometric measurements of newly discovered NEOs enabling object recovery and computation of orbital elements. Many of these efforts would not be possible without the financial support of the NASA Planetary Defense Coordination Office, for which we are grateful.

ORCID iDs

Joseph R. Masiero  <https://orcid.org/0000-0003-2638-720X>
 J. M. Bauer  <https://orcid.org/0000-0001-9542-0953>
 R. M. Cutri  <https://orcid.org/0000-0002-0077-2305>
 E. Kramer  <https://orcid.org/0000-0003-0457-2519>
 E. L. Wright  <https://orcid.org/0000-0001-5058-1593>

References

- Alí-Lagoa, V., Lionni, L., Delbo, M., et al. 2014, *A&A*, **561**, A45
 Bauer, J. M., Stevenson, R., Kramer, E., et al. 2015, *ApJ*, **814**, 85
 Benner, L. A. M., Busch, M. W., Giorgini, J. D., Taylor, P. A., & Margot, J.-L. 2015, in *Asteroids IV*, ed. P. Michel, F. E. DeMeo, & W. F. Bottke (Tucson, AZ: Univ. Arizona Press), 165
 Benner, L. A. M., Hudson, R. S., Ostro, S. J., et al. 1999, *Icar*, **139**, 309
 Busch, M. W., Benner, L. A. M., Ostro, S. J., et al. 2008, *Icar*, **195**, 614
 Busch, M. W., Giorgini, J. D., Ostro, S. J., et al. 2007, *Icar*, **190**, 608
 Chapman, C. R., Harris, A. W., & Binzel, R. 1994, in *Hazards Due to Comets and Asteroids*, ed. T. Gehrels, M. S. Matthews, & A. Schumann (Tucson, AZ: Univ. Arizona Press), 537
 Cutri, R. M., Mainzer, A., Conrow, T., et al. 2015, Explanatory Supplement to the NEOWISE Data Release Products, <http://wise2.ipac.caltech.edu/docs/release/neowise/expsup>
 Cutri, R. M., Wright, E. L., Conrow, T., et al. 2012, Explanatory Supplement to the WISE All-Sky Data Release Products, <https://wise2.ipac.caltech.edu/docs/release/allsky/expsup/index.html>
 Delbo', M., dell'Oro, A., Harris, A. W., et al. 2007, *Icar*, **190**, 236
 Hanuš, J., Delbo', M., Durech, J., & Alí-Lagoa, V. 2018, *Icar*, **309**, 297
 Hanuš, J., Delbo', M., Vokrouhlický, D., et al. 2016, *A&A*, **592**, A34
 Harris, A. W. 1998, *Icar*, **131**, 291
 Harris, A. W., & Drube, L. 2014, *ApJL*, **785**, 4
 Harris, A. W., & Drube, L. 2020, *ApJ*, **901**, 140
 Harris, A. W., Mueller, M., Delbo', M., et al. 2007, *Icar*, **188**, 414
 Hudson, R. S., & Ostro, S. J. 1995, *Sci*, **270**, 84
 Hudson, R. S., & Ostro, S. J. 1999, *Icar*, **140**, 369
 Jimenez, N., Howell, E. S., & Nolan, M. C. 2010, *BAAS*, **42**, 1056
 Koren, S. C., Wright, E. L., & Mainzer, A. 2015, *Icar*, **258**, 82
 Lawrence, K., & Benner, L. 2020, Radar shape models of asteroids compiled by Lawrence V1.0. urn:nasa:pds:gbo.ast.jpl.radar.shape_models::1.0. NASA Planetary Data System, <https://sbn.psi.edu/pds/resource/jplradarshape.html>
 Magri, C., Howell, E. S., Nolan, M., et al. 2011, *Icar*, **214**, 210
 Mainzer, A. 2019, NEOWISE Diameters and Albedos V2.0. urn:nasa:pds:neowise_diameters_albedos::2.0. NASA Planetary Data System, <https://sbn.psi.edu/pds/resource/neowisediam.html>
 Mainzer, A. K., Bauer, J., Grav, T., et al. 2014, *ApJ*, **792**, 30
 Mainzer, A. K., Bauer, J. M., Grav, T., Masiero, J., et al. 2011a, *ApJ*, **731**, 53
 Mainzer, A. K., Grav, T., Bauer, J. M., Masiero, J., et al. 2011b, *ApJ*, **743**, 156
 Mainzer, A. K., Grav, T., Masiero, J., et al. 2011c, *ApJ*, **741**, 90
 Mainzer, A. K., Grav, T., Masiero, J., Bauer, J. M., et al. 2011d, *ApJ*, **736**, 100
 Masiero, J. R., Carruba, V., Mainzer, A., et al. 2015, *ApJ*, **809**, 179
 Masiero, J. R., Mainzer, A. K., Bauer, J. M., et al. 2020, *PSJ*, **1**, 5
 Masiero, J. R., Mainzer, A. K., Grav, T., et al. 2011, *ApJ*, **741**, 68
 Masiero, J. R., Nugent, C. R., Mainzer, A. K., et al. 2017, *AJ*, **154**, 168
 Masiero, J. R., Wright, E. L., & Mainzer, A. K. 2019, *AJ*, **158**, 97
 Masiero, J. R., Wright, E. L., & Mainzer, A. K. 2021, *PSJ*, **2**, 32
 Mommert, M., Hora, J., & Harris, A. W. 2014, *ApJ*, **781**, 25
 Mommert, M., Hora, J., Trilling, D., et al. 2020, *PSJ*, **1**, 12
 Mommert, M., Jedicke, R., & Trilling, D. E. 2018, *AJ*, **155**, 74
 Naidu, S., Margot, J. L., Taylor, P. A., Nolan, M., et al. 2015, *AJ*, **150**, 54
 Nesvorný, D. 2015, Nesvorný HCM Asteroid Families V3.0. EAR-A-VARGBD-5-NESVORNYFAM-V3.0. NASA Planetary Data System, <https://sbn.psi.edu/pds/resource/nesvornyfam.html>
 Novaković, B., Tsirvoulis, G., Granvik, M., et al. 2017, *AJ*, **153**, 266
 Nugent, C. R., Mainzer, A., Bauer, J. M., et al. 2016, *AJ*, **152**, 63
 Nugent, C. R., Mainzer, A., Masiero, J., et al. 2015, *ApJ*, **814**, 117
 Pravec, P., Harris, A. W., Kušnirák, P., et al. 2012, *Icar*, **221**, 365
 Rozitis, B., Ryan, A., Emery, J., et al. 2020, *SciA*, **6**, 3699
 Salisbury, J. W., & Walter, L. S. 1989, *JGR*, **94**, 9192
 Shepard, M., Margot, J.-L., Magri, C., et al. 2006, *Icar*, **184**, 198
 Spencer, J. R., Lebofsky, L. A., & Sykes, M. V. 1989, *Icar*, **78**, 337
 Taylor, P. A., Rivera-Valentín, E. G., Benner, L. A. M., et al. 2019, *P&SS*, **167**, 1
 Vereš, P., Jedicke, R., Fitzsimmons, A., et al. 2015, *Icar*, **261**, 34
 Virtanen, P., Gommers, R., Oliphant, T., et al. 2020, *NatMe*, **17**, 261
 Warner, B., Pravec, P., & Harris, A. P. (ed.) 2019, Asteroid Lightcurve Data Base (LCDB) V3.0 urn:nasa:pds:ast-lightcurve-database::3.0. NASA Planetary Data System, <https://sbn.psi.edu/pds/resource/lc.html>
 Wright, E. L., Eisenhardt, P., Mainzer, A. K., et al. 2010, *AJ*, **140**, 1868
 Yu, L. L., Yang, B., Ji, J., & Ip, W.-H. 2017, *MNRAS*, **472**, 2388